IEEE Open Journal of
Power Electronics

Received 10 November 2023; accepted 28 November 2023. Date of publication 4 December 2023;
date of current version 11 January 2024. The review of this article was arranged by Associate Editor Zhixiang Zou.

Digital Object Identifier 10.1109/OJPEL.2023.3339014

Robust Model Predictive Control of a Renewable Energy Converter Under Parametric Uncertainty Conditions

JEFFERSON S. COSTA [1,2], ANGELO LUNARDI [1,2], DARLAN A. FERNANDES [3] (Member, IEEE), AND ALFEU J. SGUAREZI FILHO [1,2] (Senior Member, IEEE)

[1]Center for Engineering, Modeling and Applied Social Sciences, Federal University of ABC, Santo André, São Paulo 09210-580, Brazil
[2]Department of Electrical Engineering, Federal University of Pará, Tucuruí, Pará 68455-901, Brazil
[3]Department of Renewable Energies Engineering of Federal University of Paraíba, João Pessoa, Paraíba 58051-900, Brazil

CORRESPONDING AUTHOR: JEFFERSON S. COSTA (e-mail: jeffersonsc@ufpa.br)

This work was supported in part by the National Council for Scientific and Technological Development - CNPq under Grant 407867/2022-8, in part by São Paulo Research Foundation - FAPESP under Grant 2022/08737-1 and 2022/00323-3, in part by Fundação de Amparo à Pesquisa do Estado de Minas Gerais - FAPEMIG under Grant APQ-03609-17, and in part by Instituto Nacional de Energia Elétrica - INERGE.

ABSTRACT The advanced control technique Model predictive control (MPC) is gaining popularity in power electronics for converters with distributed energy resources. It combines closed-loop control and minimizes errors and control effort. As a model-based control technique, MPC's performance can degrade due to plant disturbances, such as parametric errors or large perturbations in grid voltage or load current. Our research used an MPC with modulation on a converter connected to the grid with an inductive filter for integrating renewable energy sources. The margin of robust stability (RS), derived from the singular Value Decomposition (SVD), provides a theoretical investigation of the robustness of the MPC controller tuning in dependency on the cost function weight factors and the time horizons. In the experiments conducted on a 2 kW workbench, it was confirmed that the proposed controller is stable and robust in nominal and under severe parametric uncertainty conditions, addressing the power quality criteria defined in IEEE Std. 519-2014. The experimental results show that the proposed MPC controller tuning outperforms the classical PI current controller in nominal conditions and is more robust to uncertainty in the passive filter of the grid-connected converter.

INDEX TERMS Grid-connected inverter, model predictive control (MPC), parametric uncertainty, renewable energy sources (RES), robust stability.

I. INTRODUCTION

The renewable energy sources (RES) as solar PV and wind, into the electric power system is an essential option for reducing reliance on high carbon emission sources, such as oil derivatives and coal, which contribute significantly to global warming, according to [1]. Both wind and PV have an inherent Direct Current (DC) nature, so power converters are necessary for integration into the local Alternating Current (AC) grid [2].

The most popular power converter topology used as a grid interface for RES [3] is the Voltage Source Converter (VSC) with a passive filter. According to [4], the passive filter is required to attenuate the harmonic components created by the switched voltage as well as nonlinearities such as the dead time of the VSC switches. In this work, we consider the inductive (L) filter topology due to its easy implementation as addressed in recent literature [5], [6], [7], [8]. Although higher-order filters such as inductive-capacitive (LC) or inductive-capacitive-inductive (LCL) have advantages in terms of size, cost, and attenuation of harmonic distortions, the control system design and implementation complexity increases dramatically due to characteristic resonance, which necessitates either an active or passive technique of attenuation [9], [10].

The control system of the power converter for RES integration into the electric grid must address synchronization, power and power factor regulation, harmonic distortion, and

© 2023 The Authors. This work is licensed under a Creative Commons Attribution 4.0 License. For more information, see https://creativecommons.org/licenses/by/4.0/

disturbance in grid voltage or DC bus [4], [11], [12]. The most common control technique includes the classical PI current controller [13], [14], [15], resonant proportional control (PR) [9], nonlinear controls by sliding modes or Fuzzy interface [4], state feedback [16], and MPC [17].

The MPC incorporates the characteristics of various sophisticated control approaches, such as closed-loop control, error and control effort minimization, straightforward implementation for multivariable systems, and the capacity to add physical restrictions [17], [18]. Deadbeat, Finite Control Set (FCS-MPC), Continuous Control Set (CCS-MPC), and Generalized Predictive Control (GPC) are the primary types of MPC that are gaining traction in power converter applications [4], [17], [18], [19]. The computing cost of MPC, particularly when limits are enforced, is a significant limitation [20]. Furthermore, because the MPC is a model-based technique, it may lose performance owing to parametric fluctuations and severe disturbances in load current or grid voltage, as cited by [4], [18].

The robustness is a desirable characteristic of the control techniques designed for grid-connected VSCs to reduce the effects of Total Harmonic Distortion (THD) in the grid current. Minimizing THD current waveform quality concentrates useful power in the fundamental component, indirectly improving energy conversion efficiency [21]. As more renewable energy sources are integrated via power converters and non-linear electronic loads are used by local customers, it's common for grid-connected VSCs to operate under plant disturbances like parametric errors or distorted grid voltage [3], [12], [22], [23]. The VSC control system must be capable of mitigating the impact of disturbances to improve power quality injected into the grid.

Several studies have been conducted to improve the robustness of VSC control systems. One such effort, presented in [24], developed a robust MPC with a Kalman filter observer to counter model mismatches. In another study [25], a robust Sliding Mode Controller (SMC) was designed, which performed well even in the presence of model parameter mismatch and disturbances in the grid voltage. Robust H_∞ controllers were developed in [26], [27], [28] using Linear Matrix Inequalities to solve the H_∞ norm optimization problem, considering different performance criteria. Additionally, an Active Disturbance Rejection Control (ADRC) was developed in [29] for the inner current control loop of a VSC. This method considers an extended state when accounting for disturbances, and it showed good performance in terms of disturbance rejection and fast response.

A recently published article in [6] aims to contribute to the existing literature on a specific problem. The article proposes the use of an MPC that employs a state-space model with PWM modulation for an L-filtered VSI connected to a distorted voltage grid. The authors demonstrate that the system can effectively attenuate harmonic components and meet the IEEE standard 519-2014, with THD less than 5%. However, the proposed method has some drawbacks, such as high computational cost and the need for empirical adjustment applied to the controller. These controllers are designed to eliminate the impact of harmonic elements on grid voltage. It is crucial to note that understanding harmonic components is essential for mitigating distortion.

This paper presents an explicit analysis of the stability and robustness of the CCS-MPC controller applied to grid-connected VSC with L-filter, in the synchronous rotation frame. This system serves as a grid interface for distributed RES, particularly during disturbances, contributing to applied control of power converters and energy transition. The RS margin, derived from SVD spectral gain for multi-variable systems, provides a theoretical investigation of the robustness of the CCS-MPC controller tuning under parametric uncertain and grid voltage disturbance [30], [31], [32].

The study of MPC type controller using the singular values began in our research group with the publication [33]. The authors analyzed the MPC in conjunction with the repetitive controller (PRC, Predictive Repetitive Control) by varying the parameters of the Double Fed Induction Generator (DFIG) for wind generation. In the recent publication [34], the researchers noted the potential of using SVD for analyzing the stability and robustness of the MPC control system. The authors also applied the RPC technique to achieve zero stationary error in the current internal loop and improve the robustness of the grid-connected inverter under parametric uncertainty and disturbances in grid voltage.

In this study, the authors applied the expertise of SVD robustness analysis to the CCS-MPC controller. A detailed examination of the MPC parameters' time horizons and the cost function weighting matrix is conducted. The effect of time horizons and the cost function weighting matrix selection on the dynamic behavior of the closed-loop system for an MPC in direct power control was initially investigated in [35], but only in the nominal conditions of the plant. In Table 1, we highlight the differences between this paper and other studies conducted by the group.

The stiff voltage grid model is used for small-scale applications, resulting in minimal impact of grid impedance on system stability [36]. The cost function's block diagonal matrices are reduced to identical diagonal matrices for simplicity. The main contributions of this article are presented below.

- Explicitly analysis of the stability and robustness of CCS-MPC controller applied to VSCs serving as grid interfaces for distributed RES.
- Experimental validation of the MPC controller's robust stability even under severe parametric uncertainty.
- In nominal conditions, the MPC controller tuning improves power quality.
- Experimental comparison with the classical PI current controller showed that the proposed controller had greater robustness.

The structure of this paper is as follows: Section II presents the discrete model of the plant. In Section III, we describe the CCS-MPC control technique. Section IV presents the RS analysis of the CCS-MPC controller. The experimental robustness tests are provided in Section V. The main results are summarized in Section VI.

TABLE 1. Comparing This Paper to the Group's Other Studies

Author	Plant	Control Description	Stability and Robustness Analyze
[33]	Double Fed Induction Generator (DFIG)	Current Control, MPC + Repetitive Control (RPC), PWM Modulation, Synchronous rotation frame	Applied the SVD analyze the DFIG stability under a finite set of the parametric variation.
[35]	Grid-connected Inverter + L-Filter	Direct Power Control, MPC with Modulation in synchronous rotation frame.	Applied the close loop poles analysis to evaluate the stability of the plant only in nominal conditions.
[34]	Grid-connected Inverter + L-Filter	Current Control, MPC + Repetitive Control (RPC), PWM Modulation, Synchronous rotation frame.	Applied the SVD analysis to evaluate how the RPC controller tuning affects the robustness under parametric uncertain and grid voltage disturbance.
This paper	Grid-connected Inverter + L-Filter	Current Control, MPC with Modulation in synchronous rotation frame.	Applied the SVD analysis to evaluate how the MPC controller tuning affects the robustness under parametric uncertain and grid voltage disturbance.

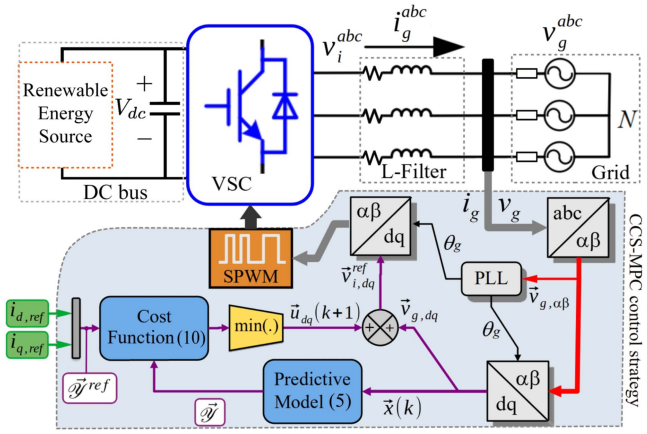

FIGURE 1. Space vector CCS-MPC strategy for the grid-connected VSC with L-filter using rotation frame *dq*.

II. MODEL OF THE VSC IN ROTATION FRAME *dq*.

The grid-connected power converter (Fig. 1) is made up of a VSC and an L-filter [12], [18]. By modulating the voltage V_{dc} into a three-phase waveform $\vec{v}_g^{abc}$ timed with the grid common connection point (CCP), the VSC injects energy into the grid from the DC bus [37]. The system's entire functionality (Fig. 1) is dependent on the VSC switches being properly driven by the space vector MPC control method in rotation frame dq [17]. The MPC employs a predictive model, as specified in section III, as well as a cost function of the tracking error of $i_{g,q}$ and $i_{g,d}$, as well as the control effort $\vec{u}_{dq}$ [38]. The crucial step is to minimize the cost function, which produces the reference signal for driving the VSC in the form $\vec{v}_i^{ref}(k) = \vec{u}_{dq}(k) + \vec{v}_{g,dq}(k)$ (Fig. 1). After converting to the $\alpha\beta$ stationary frame, a space vector PWM modulator (SPWM) drives the VSC switch from the $\vec{v}_{i,dq}^{ref}$ signal [17].

The design of the filter L_g was based in (1), as proposed by [10]. Here, $\Delta\mathcal{I}$ is the desired change of current in the inductor, f_{sw} is the switching frequency, and V_{RMS} is the effective value of the fundamental grid voltage.

$$L_g = \frac{V_{RMS}}{2\sqrt{6} f_{sw} \Delta\mathcal{I}} \tag{1}$$

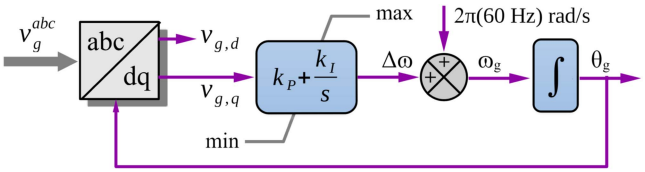

FIGURE 2. Block diagram representing the operation of the PLL.

A PLL, as shown in Fig. 2, performs grid voltage synchronization, which is a simple and robust control loop that calculates the instantaneous phase θ_g [39]. The control loop (Fig. 2) requires the measurement of three-phase currents ($\vec{i}_g^{abc}$) and voltages ($\vec{v}_g^{abc}$) at the grid CCP, which are transformed to the synchronous frame dq first using the Clarke transform and then using θ_g and the Parke transform [40]. The grid voltage vector $\vec{v}_{g,dq}$ and the d-axis of the rotating frame dq are forced into synchronism in the PLL (Fig. 2) at the same angle θ_g as estimated by the PI control loop, so that the Parke transform results in $v_{g,q} = 0$ and $|\vec{v}_{g,dq}| = v_{g,d}$ [39]. Because it permits individual management of active power P and reactive power Q by employing only the components $i_{g,d}$ and $i_{g,q}$, as established in (2) [17], this technique produces a weak coupling between the d and q components of the system variables.

$$\begin{aligned} P &= \frac{3}{2}\Re\left\{\vec{v}_{g,dq}\,\vec{i}^{*}_{g,dq}\right\} = \frac{3}{2} v_{g,d}\, i_{g,d} \\ Q &= \frac{3}{2}\Im\left\{\vec{v}_{g,dq}\,\vec{i}^{*}_{g,dq}\right\} = -\frac{3}{2} v_{g,d}\, i_{g,q} \end{aligned} \tag{2}$$

(3) presents the continuous-time model for the VSC in the dq frame. The zero-order holder (ZOH) is used to approximate the derivative of the current in (3) in order to create the discrete-time model [41]. In (4), the outcome of the formula manipulation is displayed, and in (5), the compact model terms are identified by square brackets. In (4) $\vec{u}_{dq} = \vec{v}_{i,dq} - \vec{v}_{g,dq}$ is an auxiliary variable that represents the difference between VSC and network voltages [42]. In (5) C_{dis} is an identity matrix 2×2.

$$\begin{bmatrix} \frac{\mathrm{d}i_{g,d}}{\mathrm{d}t} \\ \frac{\mathrm{d}i_{g,q}}{\mathrm{d}t} \end{bmatrix} = \begin{bmatrix} -\frac{R}{L} & -\omega_g \\ \omega_g & -\frac{R}{L} \end{bmatrix} \begin{bmatrix} i_{g,d} \\ i_{g,q} \end{bmatrix}$$

$$+\begin{bmatrix}\frac{1}{L} & 0\\ 0 & \frac{1}{L}\end{bmatrix}\begin{bmatrix}v_{i,d}-v_{g,d}\\ v_{i,q}-v_{g,q}\end{bmatrix} \tag{3}$$

$$\overbrace{\begin{bmatrix}i_{g,d}(k+1)\\ i_{g,q}(k+1)\end{bmatrix}}^{\vec{x}(k+1)}=\overbrace{\begin{bmatrix}1-\frac{RT_s}{L} & -\omega_g T_s\\ \omega_g T_s & 1-\frac{RT_s}{L}\end{bmatrix}}^{A_{dis}}\overbrace{\begin{bmatrix}i_{g,d}(k)\\ i_{g,q}(k)\end{bmatrix}}^{\vec{x}(k)}+\underbrace{\begin{bmatrix}\frac{T_s}{L} & 0\\ 0 & \frac{T_s}{L}\end{bmatrix}}_{B_{dis}}\underbrace{\begin{bmatrix}v_{i,d}-v_{g,d}\\ v_{i,q}-v_{g,q}\end{bmatrix}}_{\vec{u}_{dq}(k)} \tag{4}$$

$$\begin{aligned}\vec{x}(k+1)&=A_{dis}\vec{x}(k)+B_{dis}\vec{u}_{dq}(k)\\ \vec{y}(k+1)&=C_{dis}\vec{x}(k+1).\end{aligned} \tag{5}$$

III. MPC CONTROL FOR GRID-CONNECTED VSC

The MPC strategy's predictive model (Fig. 1) employs model from (5) to forecast the future behavior of power injected into the grid up to the sliding horizon n_y [38], [43]. The predictive model in (6) is formed by successive applications of (5), where: $\vec{\mathcal{Y}} \in \Re^{n_y\times 2}$ is the prediction vector of the system output defined in (7); $\vec{x}(k)$ are the actual measurements of the state variables; $U \in \Re^{2n_u\times 1}$ is the prediction vector of the control signal up to the horizon n_u defined in (9); Ψ is the predictive state matrix defined in (10).

$$\vec{\mathcal{Y}} = \Psi\,\vec{x}(k) + \mathcal{M}\,U \tag{6}$$

$$\vec{\mathcal{Y}} = \begin{bmatrix}\vec{y}(k+1) & \vec{y}(k+2) & \cdots & \vec{y}\left(k+n_y\right)\end{bmatrix}^\top \tag{7}$$

$$U = \begin{bmatrix}\vec{u}_{dq}(k+1) & \vec{u}_{dq}(k+2) & \cdots & \vec{u}_{dq}(k+n_u)\end{bmatrix}^\top \tag{8}$$

$$\Psi = \begin{bmatrix}C_dA_d & C_dA_d^2 & C_dA_d^3 & \cdots & C_dA_d^{n_y}\end{bmatrix}^\top \tag{9}$$

$$\mathcal{M} = \begin{bmatrix} C_dB_d & \mathbf{0} & \cdots & \mathbf{0}\\ C_dA_dB_d & C_dB_d & \cdots & \mathbf{0}\\ C_dA_d^2B_d & C_dA_dB_d & \cdots & \mathbf{0}\\ \vdots & \vdots & \ddots & \vdots\\ C_dA_d^{n_y-1}B_d & C_dA_d^{n_y-2}2B_d & \cdots & C_dB_d\end{bmatrix} \tag{10}$$

A. COST FUNCTION

The quadratic cost function in (11) uses the predictions of the reference $\vec{\mathcal{Y}}^{ref} \in \Re^{2n_y\times 1}$, the system output (6) and the control signal (8) [38]. The terms Γ_y and Γ_u in (11) are diagonal weighting matrices of the tracking error and the control effort, respectively.

$$\mathcal{J} = \left(\vec{\mathcal{Y}}^{ref} - \vec{\mathcal{Y}}\right)^\top \Gamma_y \left(\vec{\mathcal{Y}}^{ref} - \vec{\mathcal{Y}}\right) + U^\top \Gamma_u U \tag{11}$$

The vector $\vec{\mathcal{Y}}^{ref}$ is defined by the reference signal $\vec{y}^{ref}(k) = \begin{bmatrix}i_{d,ref}(k), & i_{q,ref}(k)\end{bmatrix}^\top$, which is repeated n_y times in (12) through multiplication by $F = \begin{bmatrix}I & I & \cdots & I\end{bmatrix}^\top$ [18]. In this sense, the grid voltage is regarded constant within the prediction horizon n_y, which is compatible with DC values in the dq synchronous frame for any n_y. This method is utilized in [43] to define the CCS-MPC in the $\alpha\beta$ stationary frame, however it is limited to short time horizons [17].

$$\vec{\mathcal{Y}}^{ref} = F_{[2n_y\times 1]}\vec{y}^{ref}(k) \tag{12}$$

According to [18], the weight factors $\Gamma_y \in \Re^{2n_y\times 2n_y}$ and $\Gamma_u \in \Re^{2n_u\times 2n_u}$ are positive definite block diagonal matrices. To decrease the degrees of freedom associated with the MPC controller, the cost function weighting block diagonal matrices are simplified to diagonal matrices with equal terms, as shown in (13) and (14). As a result, the important parameters for MPC-DPC performance are reduced to four: γ_y, γ_u, n_y, and n_u.

$$\Gamma_y = \gamma_y\, diag\left(\begin{bmatrix}I & I & I & \cdots & I\end{bmatrix}\right) \tag{13}$$

$$\Gamma_u = \gamma_u\, diag\left(\begin{bmatrix}I & I & I & \cdots & I\end{bmatrix}\right) \tag{14}$$

B. MINIMIZATION OF THE COST FUNCTION

We do not impose constraints for the system variables in the MPC method used in this study, allowing us to get an analytical solution for minimizing the cost function (11) by solving $\partial\mathcal{J}/\partial U = 0$ [44]. The solution U presented in (15) is a control signal prediction vector, as stated in (8), with the first element being the control signal for the system's recent horizon $\vec{u}_{dq}(k)$ [42]. The control signal $\vec{u}_{dq}(k)$ can be obtained from (15) as $\mathcal{W} = \begin{bmatrix}I_{2\times 2} & \mathbf{0} & \cdots & \mathbf{0}\end{bmatrix}_{[2\times(2n_u+2)]}$.

$$U = \left(\mathcal{M}^\top\Gamma_y\mathcal{M} - \Gamma_u\right)^{-1}\mathcal{M}^\top\Gamma_y\left[\vec{\mathcal{Y}}^{ref} - \Psi\,\bar{x}(k)\right] \tag{15}$$

It should be noted that the control signal created by equation (15) provides continuous amplitude values that are applied to the SPWM, allowing the inverter to be driven with a wider range of voltage values rather than being limited to the eight voltage vectors used in standard FCS controllers [18].

A more compressible way to define the control signal $\vec{u}_{dq}(k+1)$ is presented in (16), where $\mathcal{K} = \mathcal{W}(\mathcal{M}^\top\Gamma_y\mathcal{M} - \Gamma_u)^{-1}\mathcal{M}^\top\Gamma_y$ is a constant matrix and independent of the measurements of the system variables, so can be calculated external to the real-time control loop [42]. (16) computational load is similar to that of basic state feedback [44], [45], but it accomplishes error and control effort minimization at each time instant when the reference is updated and new measurements of the state variables are available.

$$\vec{u}_{dq}(k+1) = \mathcal{K}\left[\vec{\mathcal{Y}}^{ref} - \Psi\,\bar{x}(k)\right] \tag{16}$$

IV. ROBUST STABILITY ANALYSIS

In this section, we analyze the CCS-MPC controller's robustness in the grid-connected VSC under parametric uncertainty using RS analysis. First, we verify nominal stability for various controller tuning by calculating the closed-loop eigenvalues. The details of the grid-connected VSC's nominal configuration can be found in Table 2. According to [46], the

Algorithm 1: CCS-MPC algorithm.

Result VSC switch drive.
Load the system parameters: R, L, V_{ab}, f_g, V_{dc}, f_{sw}, γ_y, γ_u, n_y, n_u;
while CCS-MPC *is active* **do**
  Data acquisition: 3-phase $\vec{i}_{g,abc}(k)$ and $\vec{v}_{g,abc}(k)$;
  Apply Clark transform: $\vec{i}_{g,\alpha\beta}(k)$ and $\vec{v}_{g,\alpha\beta}(k)$;
  Active PLL: θ_g;
  Apply Park transform: $\vec{i}_{g,dq}(k)$ and $\vec{v}_{g,dq}(k)$;
  Apply (2): $\vec{x}(k) = [i_{g,d}, i_{g,q}]$;
  Build the system model (5): A_d, B_d, and C_d;
  Build the predictive model (6): Ψ, $\mathcal{M}$ and $\mathcal{Y}_{ref}$;
  Build the cost function $\mathcal{J}$ (11);
  Minimize $\mathcal{J}$ using (16): $\vec{u}_{dq}(k)$;
  $\vec{v}_{i,dq}(k+1) = \vec{u}_{dq}(k+1) + \vec{v}_{g,dq}(k)$;
  Apply inverse Park transform: $\vec{v}_{i,\alpha\beta}(k)$);
  Apply $\vec{v}_{i,\alpha\beta}(k)$ to the SPWM modulator;
  return VSC switches states;
end

TABLE 2. Nominal Parameters of the Grid-Connected VSC

Parameter	Value
Inverter Power	2 kVA
Nominal Current	15 A
Grid Voltage (V_g)	77.8 V_{RMS}
Grid Frequency f_g	60 Hz
Switching Frequency, f_s	20 kHz
Inductance Filter L_g	13.2 mH
Resistance Filter R_g	0.1 Ω
Sampling Time, T_s	0.1 ms
Voltage DC link, V_{dc}	300 V

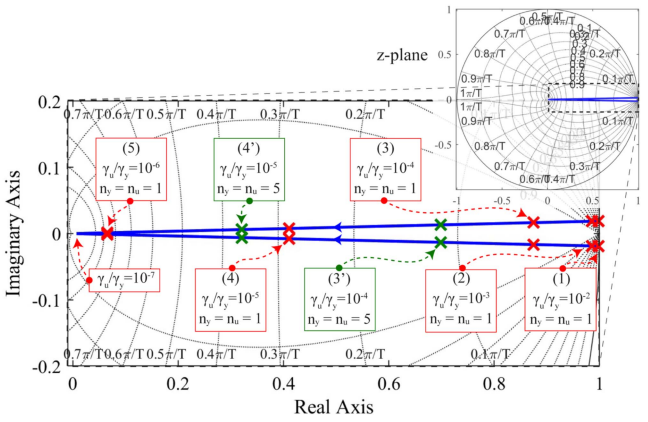

FIGURE 3. Root locus of the CCS-MPC tuning $10^{-7} \leq \gamma_u/\gamma_y \leq 10^{-1}$ and $n_y = n_u = 1$ (blue line). The red markers indicate the tunings (1) $\gamma_u/\gamma_y = 10^{-2}$; (2) $\gamma_u/\gamma_y = 10^{-3}$; (3) $\gamma_u/\gamma_y = 10^{-4}$; (4) $\gamma_u/\gamma_y = 10^{-5}$; and (5) $\gamma_u/\gamma_y = 10^{-6}$. The green markers represent the tunings for (3) and (4) with $n_y = n_u = 5$.

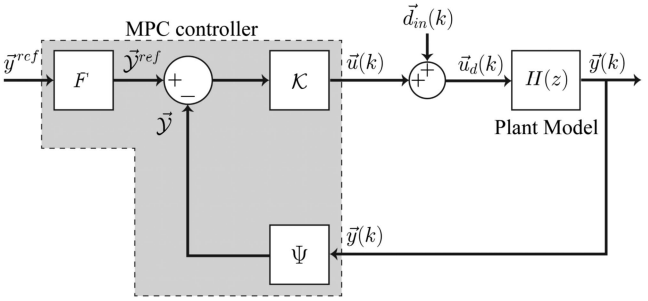

FIGURE 4. Closed-loop block diagram of the CCS-MPC controller.

eigenvalues given by (17) are the closed-loop poles of the CCS-MPC controller, which can be deduced by substituting the control law from (16) into the discrete model from (5).

$$\left|A_d - B_d \mathcal{K} \Psi - zI\right| = 0 \tag{17}$$

According to the research conducted by [23], the cost function weights are tuned by the ratio of γ_u to γ_y, which is the decisive factor in the minimum of the cost function, independent of the values of individual γ_u and γ_y. Here we adopt the tuning range of γ_u/γ_y from 10^{-7} to 10^{-1} and the time horizons $n_y = n_u = [1, 5, 10]$. The value of γ_y is set to be 10^5 arbitrarily. The CCS-MPC controller's coarse tuning involves adjusting the γ_u/γ_x ratio magnitude order. The blue curve in Fig. 3 represents the root locus of the closed-loop CCS-MPC current controller in the z-plane. It moves from the unit circle's edge to the center as the γ_u/γ_y tuning decreases.

The results in Fig. 3 show that the CCS-MPC control system is stable as the poles lie within the unit circle in the z-plane across the range of tunings examined. Additionally, it was observed that increasing the horizons n_y and n_u caused the poles to shift towards the center of the unit circle. The variations in tunings (3) and (4) when the horizons increased from $n_y = n_u = 1$ to $n_y = n_u = 5$ revealed this impact.

To explicitly evaluate the stability, we apply the definitions of the RS margin proposed by [30] to calculate the tolerable parametric uncertainty in the L-filter (ΔL_g and ΔR_g). The symbol σ represents the singular values that indicate the spectral gain for multivariable systems [31]. It helps to assess the sensitivity dynamics of the system towards changes in the model. This analysis provides valuable insights into the system's sensitivity to model variations. The RS margin is calculated from the structured singular value, which is an extension of the SVD concept [32]. This value is obtained by applying it to the sensitivity function (S) [33].

The block diagram of the closed-loop CCS-MPC control is shown in Fig. 4. In this case, $H(z)$ represents the dynamic model of the grid-connected power converter as described in section II and $\vec{d}_{in}$ represents input disturbances, e.g. parameter uncertainty and grid voltage distortion [31]. The sensitivity function S is the transfer function between the disturbance $\vec{d}_{in}$ and the plant input signal $\vec{u}_d$, as defined in (18).

$$S = [I + \mathcal{K}\Psi H(z)]^{-1} \tag{18}$$

To conduct the RS analysis, we use the plant model represented by (5) with uncertainties in the L-filter parameters (L_g and R_g) above and below the nominal values. We aim to

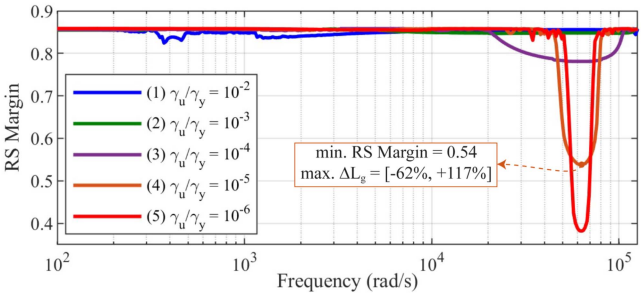

FIGURE 5. RS margin for five CCS-MPC controller tuning with $n_y = n_u = 1$.

TABLE 3. Tolerable Parametric Uncertainty Equivalent to the Minimum RS Margin

Tuning	γ_u/γ_y	Tolerable ΔL_g	Tolerable ΔR_g
(1)	10^{-2}	$[-84\%, +236\%]$	$[-81\%, +680\%]$
(2)	10^{-3}	$[-86\%, +248\%]$	$[-82\%, +778\%]$
(3)	10^{-4}	$[-81\%, +214\%]$	$[-78\%, +541\%]$
(4)	10^{-5}	$[-62\%, +117\%]$	$[-62\%, +194\%]$
(5)	10^{-6}	$[-47\%, +73\%]$	$[-49\%, +105\%]$

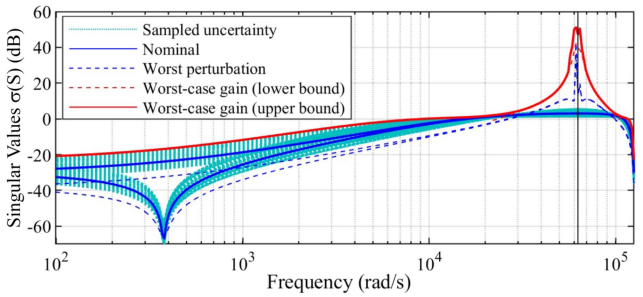

FIGURE 6. Worst disturbance analysis in the singular values $\sigma(S)$ of the CCS-MPC controller tuning (4).

determine the minimum RS margin of the closed-loop CCS-MPC control system. By doing so, we can establish the range of parametric uncertainty within which stability is ensured. Fig. 5 displays the RS margin based on frequency for the five controller tunings highlighted in Fig. 3. Table 3 lists the allowable parametric uncertainty (ΔL_g and ΔR_g).

In Fig. 5, the minimum RS margin for tuning (4) is 0.55 at the critical frequency of 62.900 rd/s or 54% of the arbitrary uncertainty interval 0.5 mH $< L_g <$ 60 mH and 0.01 $\Omega < R_g <$ 4 Ω; that is, the close-loop stability is ensured in nominal condition and under parametric uncertainty limits $[-62\%, +117\%]$ for L_g and $[-62\%, +194\%]$ for R_g. It should be noted that the CCS-MPC controller has a high level of robustness, even in cases where the nominal poles are near the unit circle (Fig. 3). For example, tuning (1) has a tolerable range of parameter variation of $[-84\%, +236\%]$ for L_g.

To study how parametric uncertainty and the RS margin impact the closed-loop PRC control system, Fig. 6 displays the worst-case analysis of the spectral gain or singular value for tuning (4) [32]. The figure reveals that even in the worst perturbation scenario (indicated by the blue dashed line), parametric uncertainty only leads to limited gain for any

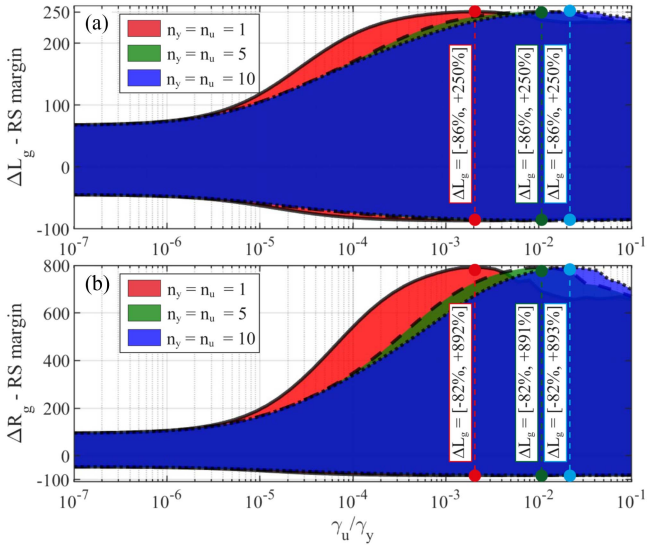

FIGURE 7. Effect of the CCS-MPC controller tuning on robust stability or tolerable parametric uncertainty in the L-filter, relative to the nominal parameter $L_g = 13.2$ mH and $R_g = 0.1$ Ω: (a) Inductance and (b) Internal Resistance.

frequency. In Fig. 6, the singular value curves that indicate the worst-case scenario are represented by the blue line for the nominal system, blue dashed lines for parametric uncertainty samples, and red line for the worst-case gain. These curves show the envelope of the worst gain for each frequency, which indicates the robust stability barrier for the spectral gain of the PRC control system, as discussed in [47].

We conducted a more detailed analysis of the minimum RS margin for different CCS-MPC controller tuning within the range of $10^{-7} < \gamma_u/\gamma_y < 10^{-1}$, building upon the RS analysis in Table 3. The resulting tolerable parametric uncertainty is presented in Fig. 7. Fig. 7 shows that the robust stability of the CCS-MPC controller is maximum for the tuning range $10^{-3} < \gamma_u/\gamma_y < 10^{-2}$ with $n_y = n_u = 1$, thus being able to maintain stability under parametric uncertainty up to the limits $[-86\%, +250\%]$ for L_g and $[-82\%, +892\%]$ for R_g. It is noteworthy that the maximum tolerance for parametric uncertainty remains relatively stable for longer time horizons ($n_y = n_u = 5$ and $n_y = n_u = 10$). However, it is crucial to consider that the γ_u/γ_y tuning for maximum robustness varies depending on the time horizon. The results in Fig. 7 show that the CCS-MPC control system maintains robust stability against parametric uncertainty ranging from a decrease of 44% to an increase of 67% in the L-filter inductance.

A. ROBUSTNESS TO GRID VOLTAGE DISTURBANCE

To ensure the stability of the proposed control system, it is important to consider the impact of disturbances in the grid voltage. This can be achieved by examining the input signal components of the plant described in (5), as shown in the frequency response depicted in Fig. 8. The disturbance we will be considering the uncertainty in the amplitude of the fundamental component, ranging from -100% to 100%,

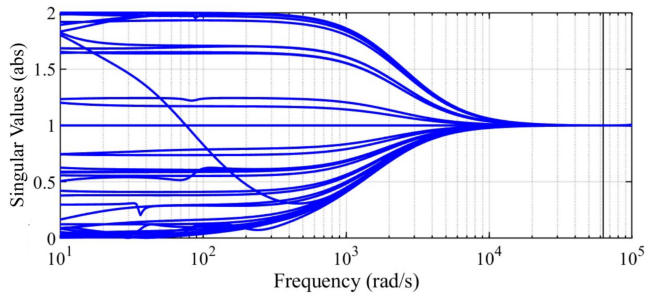

FIGURE 8. Spectral profile of the grid voltage disturbance.

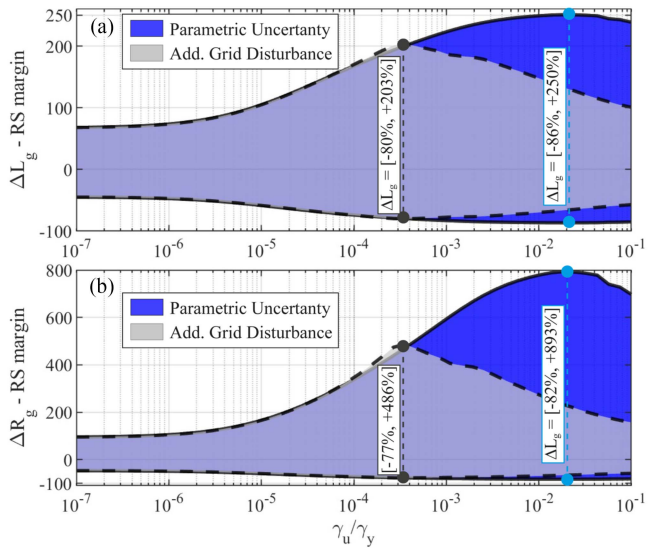

FIGURE 9. Minimum RS margin of the CCS-MPC controller under grid voltage disturbance.

as well as distortions caused by harmonic components up to the 19th order [6]. This level of uncertainty in the grid voltage is significant and can be compared to contingencies, such as harmonic distortions or voltage sag.

The effect of the grid voltage disturbance in the minimum RS margin of the CCS-MPC controller is shown in Fig. 9. In this case, the time horizons were fixed at $n_y = n_u = 10$. In general, the minimum robust stability margin becomes narrower due to input signal disturbance, especially for tunings where the ratio γ_u/γ_y is greater than 3.5×10^{-4} and the critical frequencies of $\sigma(S)$ are within the input disturbance band, as shown in Fig. 5. The maximum stability margin for the L-filter inductance is reduced from $[-86\%, +250\%]$ to $[-80\%, +203\%]$ when the grid voltage distortion is considered. The RS margin in $\gamma_u/\gamma_y \leq 3.5 \times 10^{-4}$ is similar to that case where only the parametric uncertainty is analyzed. Curiously, in the worst case at $\gamma_u/\gamma_y = 10^{-6}$, the distortion in the grid does not significantly impact the robustness margin of the controller. This suggests that with the correct tuning of the CCS-MPC controller, stability can be ensured in nominal conditions and theoretically accommodate a variation in the L-filter inductance of up to $\pm 40\%$.

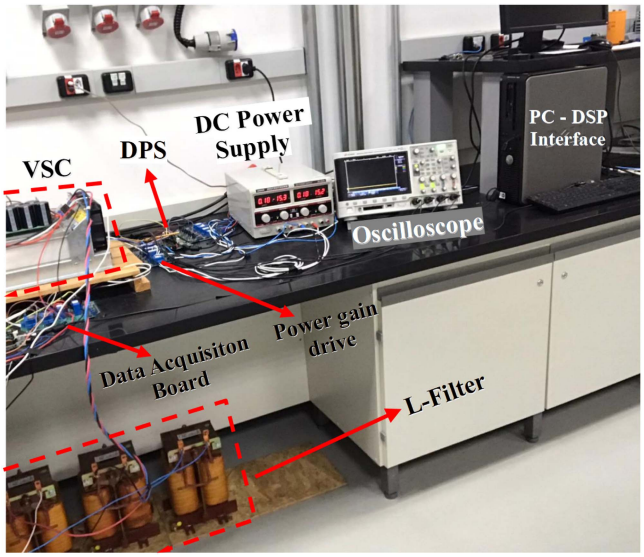

FIGURE 10. Workbench for experimental validation purposes.

V. EXPERIMENTAL RESULTS OF THE CCS-MPC CONTROLLER

In this paper, we obtained our results using the experimental 3-phase bench presented in Fig. 10. The bench consists of several main components, including an electronic board for conditioning the three-phase voltage and current, a DSP Texas Instruments model TMS320F28335 to run control algorithms, a 2 kVA/800 Vdc/380 Vac three-phase/two-level power converter, a 13.5 mH inductive bank (L-filter), and an AC programmable power supply model SUPPLIER FCATHQ 4500 VA/380 V/500 Hz to simulate the power grid [41]. The setup for the grid-connected VSC experiment is identical to the one outlined in Table 2.

We used the integral square error (ISE) to measure power regulation, which is defined in (19) [31]. We also calculated the quality of energy injected into the grid using the total harmonic distortion (THD). Equation (19) defines $\vec{e}$ as the error vector for active and reactive power reference tracking, which is equal to $[P_g - 1.5V_g i_{g,d}^{ref}, Q_g + 1.5V_g i_{g,q}^{ref}]^\top$. It is recommended by the IEEE 519-2014 standard [48] that the THD should not exceed 5%.

$$ISE = \|\vec{e}(t)\|_2 = \sqrt{\int_0^\infty |\vec{e}(\tau)|^2 \, d\tau}. \tag{19}$$

A. TUNING THE CCS-MPC UNDER NOMINAL CONDITIONS

Experimental tests in this section were conducted to compare the performance of four different CCS-MPC controller tunings numbered (2) through (5) with $n_y = n_u = 1$. Tuning (4) had a γ_u/γ_y value of 10^{-5} and the resulting measurements for the $i_{g,d}$ and $i_{g,q}$ components of the grid current are shown in Fig. 11. Fig. 12 compares the AC current and voltage measured at the grid connection point. The experimental performance was evaluated with ISE = 10.36 dB and THD = 1.07%. Tuning (3) had a γ_u/γ_y value of 10^{-4} and Fig. 13

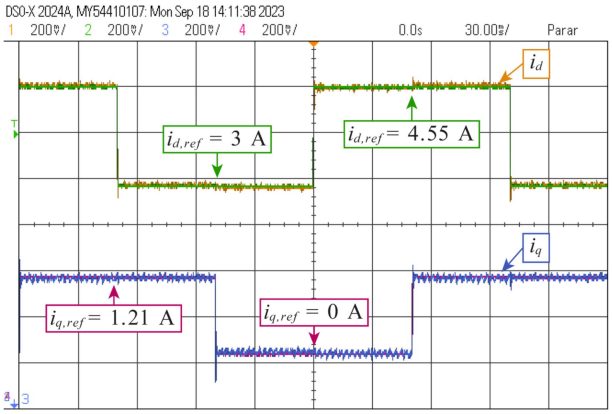

FIGURE 11. Measurements using the CCS-MPC tuning (4): components $i_{g,d}$ and $i_{g,q}$ of the grid current.

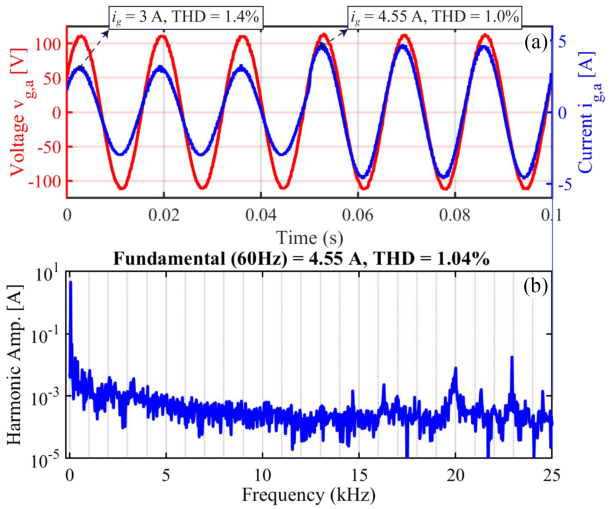

FIGURE 12. (a) Measurements using CCS-MPC tuning (4): AC current and voltage in the grid phase; (b) Spectral components of the AC current ($i_{g,d}^{ref}$ = 4.55 A and $i_{g,q}^{ref}$ = 0 A).

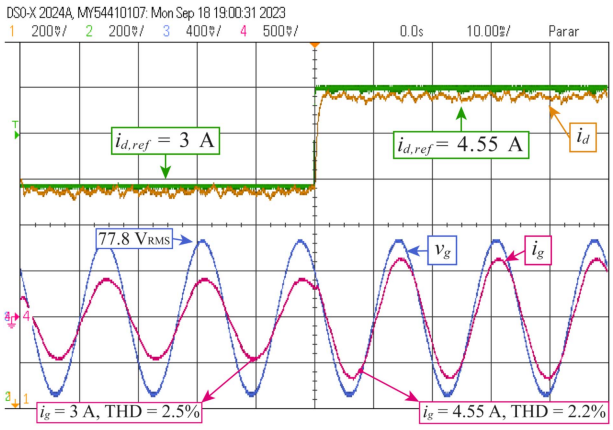

FIGURE 13. Measurements using the CCS-MPC tuning (3): d-axis current $i_{g,d}$ and reference, and the AC current and voltage in the grid phase.

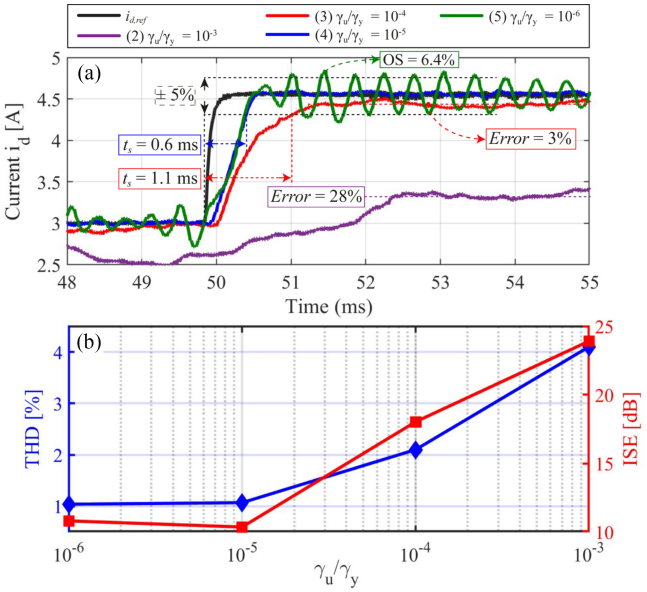

FIGURE 14. Comparison of the CCS-MPC controller performed using tunings (2) through (5): (a) Step response of d-axis grid current; (b) power quality ISE and THD.

shows the experimental results for the d-axis current component $i_{g,d}$ and the AC current and phase voltage in the grid. For the tunings (3) and (4), the CCS-MPC controller guarantees the nominal stability and the power quality performance (THD below 5%) for at least 3 A current reference, equivalent to 20% of the converter's nominal power.

To better compare the performance of the CCS-MPC controller tuning experimentally, Fig. 14 displays the step response of the grid current $i_{g,d}$, as well as the ISE and THD performances. Note that although tuning (2) shows nominal stability of the control system, it has a very large steady-state error (-30%). Although the ISE and THD performances of Tunings (4) and (5) are similar in Fig. 14(b), Tuning (5) exhibits a strong oscillation (± 6.5%) around the reference in the permanent regime as shown in Fig. 14(a). In addition, tuning (3) has a slight regime error and a slower transition compared to tuning (4). Moreover, tuning (4) has better power quality performance in terms of ISE and THD. Overall, CCS-MPC tuning with $\gamma_u/\gamma_y = 10^{-6}$ and $n_y = n_u = 1$ showed the best nominal performance.

The purpose of the results shown in Fig. 15 is to study how different time horizons affect the performance of the CCS-MPC controller tuning. It is worth noting that when the value of n_y is increased from 1 to 10 for tuning (2) and (3), there is a significant improvement in both ISE and THD performance. However, the effect of the time horizon is less pronounced for tuning (4) and (5). Fig. 15 indicates that tuning (4) consistently produces the best ISE performance, regardless of the time horizon. Furthermore, when $n_y = n_u = 10$, tuning (4) achieves a THD performance of 0.91%, which is superior to tuning (5). Based on extensive experimentation, it has been determined that the optimal ISE and THD performance can

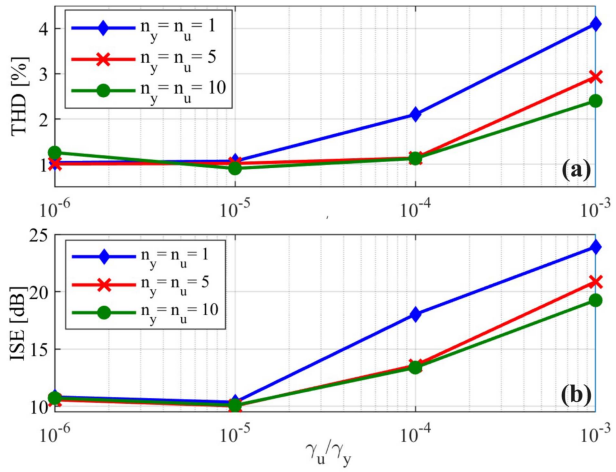

FIGURE 15. Effect of the time horizons in the performance of the CCS-MPC controller tuning: (a) THD and (b) ISE.

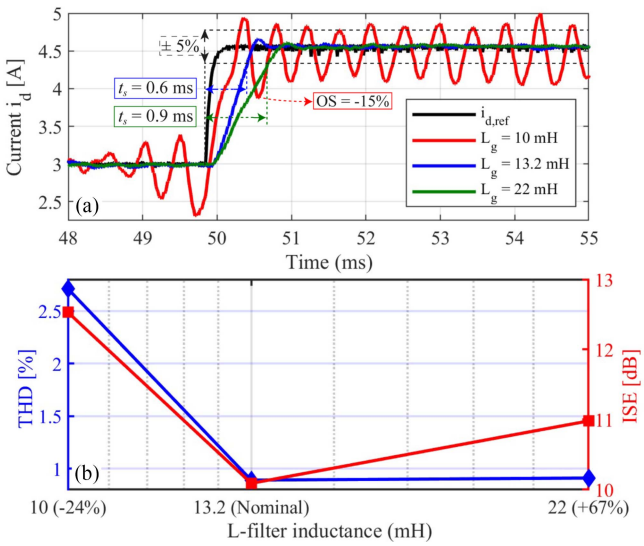

FIGURE 16. Performance of the CCS-MPC controller under parametric uncertainty: (a) Step response of d-axis grid current; (b) power quality ISE and THD.

be achieved by using the CCS-MPC tuning values of $\gamma_u/\gamma_y = 10^{-5}$ and $n_y = n_u = 10$.

B. VALIDATION OF THE ROBUSTNESS OF THE CCS-MPC CONTROLLER

This section presents the experimental validation of the CCS-MPC controller's robust stability under parametric variation in the L-filter. In the experiments, the nominal inductor of 13.2 mH was replaced by two others with values of 10 mH and 22 mH, corresponding to relative variations of -24% and +67%, respectively. These parametric deviations are within the stability margin for the controller tuning in $\gamma_u/\gamma_y = 10^{-5}$ and $n_y = n_u = 10$, estimated in $[-58\%, +105\%]$ (Fig. 7). The d-axis step response under parametric variation is compared to the nominal case in Fig. 16(a), highlighting the performance metrics in transitory. Fig. 16(b) shows the ISE and THD power quality performance.

The results in Fig. 16(a) show that the CCS-MPC controller can track current references for parametric variations of -24% and $+67\%$, which validate the robust stability of the proposed tuning. The blue line representing nominal transient performance (Fig. 16(a)) deteriorates significantly when the inductance of the L filter decreases, resulting in a strong current oscillation around the reference ($\pm$ 10% in red line) and lower power quality or higher ISE and THD (Fig. 16(b)). Note that as the filter inductance increases, the current response in Fig. 16(a) becomes slower, resulting in a lower t_s. The ISE degrades with an increase or decrease in L-filter inductance, while THD remains close to nominal during testing with the 22 mH inductor. The proposed PRC controller delivers a sinusoidal current with less than 5

C. PERFORMANCE COMPARISON WITH CLASSICAL CONTROL TECHNIQUES

In this section, we are comparing the robustness of the CCS-MPC controller tuning that is proposed in this paper with the classical PI controller in the synchronous rotation frame. To design the PI, we applied the well-established method proposed by [21] for the current control of a grid-connected VSC with L-filter. The method suggests using the gains $k_p = L_g/\tau_i$ and $k_i = T_s R_g/\tau_i$ from the parameter τ_i. The parameter τ_i represents the time constant of the approximation of the closed-loop dynamics of the control system with a first-order model. It should be selected to be small for a fast response but large enough to ensure that the closed-loop bandwidth $(1/\tau_i)$ is smaller than the PWM switching frequency (20 kHz) [21]. Through experimental testing, the PI controller's tuning was evaluated to determine its best performance in both transient and power quality ISE and THD. This is illustrated in Fig. 17. In Fig. 17(a), the measurements of the step response of the component current d injected into the network are displayed. Fig. 17(b) summarizes the ISE and THD performance for the tested tunings of the parameters τ_i. The results indicate that the PI's ISE and THD performance improves when the τ_i parameter is reduced to 100 μs, as even lower values tend to generate lower performance. Moreover, the PI with tuning at $\tau_i = 100\mu$s has the best settling time ($t_s = 1$ ms) and the lowest overshoot (13%). It is worth noting that 14% is still too high when compared to the overshoot level of the best tuning of the CCS-MPC (blue line in Fig. 14). Nevertheless, the best tuning of the PI controller with $\tau_i = 100\mu$s generates the gains $k_p = 132$ and $k_i = 0.25$ and results in a phase margin of 75° and gain margin of 12 dB [13].

The robustness tests of the designed PI were performed using the same parametric uncertain $\Delta L_g = [-24\%, +67\%]$ of the grid-connected VSC with L-filter described in section V-B. The step response for the PI controller is presented in Fig. 18(a) and Fig. 18(b) compares the robustness under parametric uncertainty of the PI with the proposed CCS-MPC controller tuning. The graph shown in Fig. 18(b) displays the nominal performance of the controllers when $L_g = 13.2$ mH

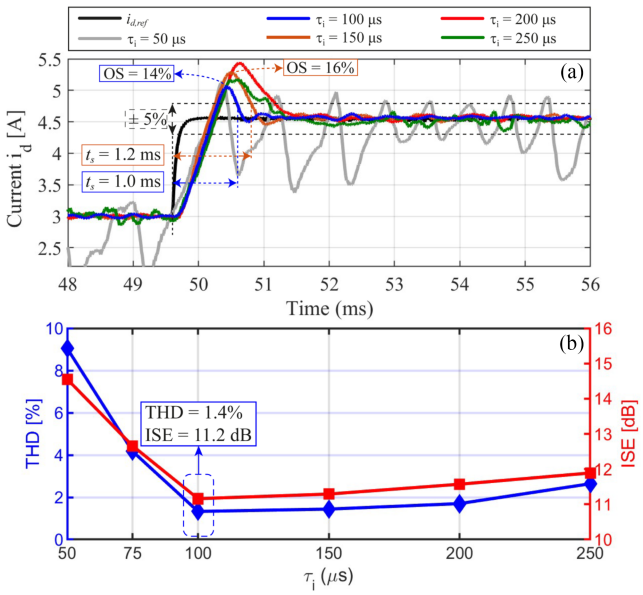

FIGURE 17. **Experimental measurements of the PI controller tuning: (a) Step response of d-axis grid current; (b) power quality ISE and THD.**

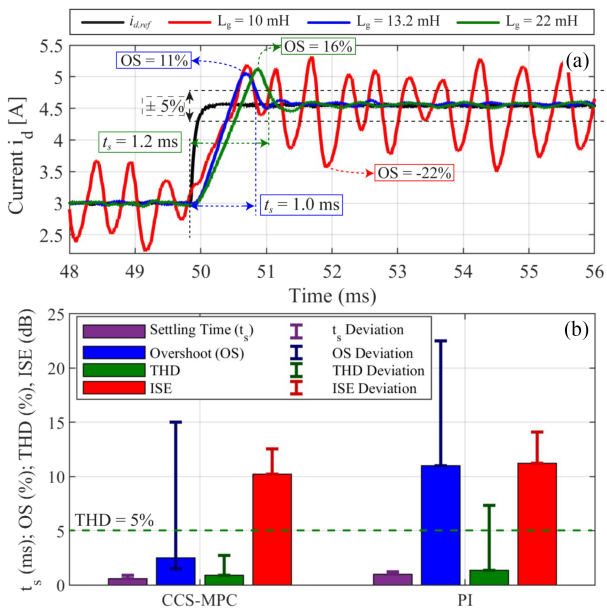

FIGURE 18. **(a) Grid current response for the designed PI under parametric uncertainty; (b) Robustness comparison of the proposed CCS-MPC and PI.**

through the height of the bars. The error lines indicate how parametric variations affect the performance metrics, which tend to worsen all aspects except for the overshoot of the CCS-MPC controller. In the case of $L_g = 22$ mH, the overshoot decreases during the testing of the CCS-MPC.

The grid current curves in Fig. 18 indicate that the PI's performance reduces significantly when the L filter's inductance is lowered. The PI's ability to follow the reference decreases more than that of the CCS-MPC in Fig. 16. In comparison to the CCS-MPC controller proposed in this article, the PI

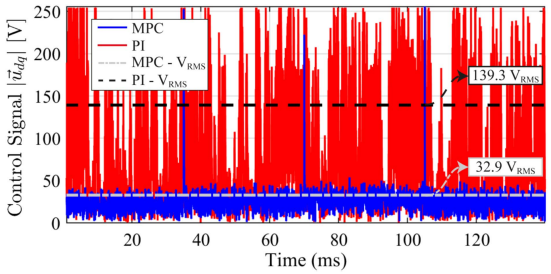

FIGURE 19. **Comparison of the control effort between the MPC and PI methods.**

controller displayed inferior performance in ISE and THD during the robustness test. The CCS-MPC controller performs well under nominal conditions and is more robust to variations in the L-filter for grid-connected VSC. Additionally, the PI's performance deviation goes beyond the minimum THD performance, with values exceeding 5%, which violates the IEEE 519-2014 standard.

It is important to note that the PI controller is not designed to minimize the control effort as effectively as the MPC [15]. The control effort of the MPC and PI methods are compared in Fig. 19. The MPC control effort (32.9 Vrms) is significantly lower than the PI controller (139.3 Vrms), indicating the efficiency gains achieved through our proposed approach [18]. In our efficiency comparison, our tests showed that CCS-MPC takes 31 microseconds to run, while PI takes 30 microseconds. Therefore, both controllers perform very similarly in terms of computational cost.

VI. CONCLUSION

In this paper, we propose a robust CCS-MPC controller for a grid-connected VSC with an L-filter to integrate renewable energy sources. We examined the robust stability of the CCS-MPC controller under different cost function weight factors and time horizons using the generalized singular values derived from SVD. We found that the controller was stable under all the different tunings we tested, even under severe grid voltage disturbances and uncertainties of up to ±40% in the L-filter inductance.

The effectiveness of the CCS-MPC controller tuning was tested on a 2 kW experimental bench. The best performance in terms of the quality of energy injected into the grid was achieved with a time horizon of 10 for the cost function weight factors $\gamma_u/\gamma_y = 10^{-5}$. Parametric tests were conducted using inductances of 10 mH and 22 mH, which varied from -24% to +67% of the rated L-filter value. These tests verified the CCS-MPC controller's robust stability under parametric uncertainty. The CCS-MPC controller outperforms the classical PI current controller under nominal conditions and is more robust to variations in the L-filter for grid-connected VSC.

REFERENCES

[1] V. Masson-Delmotte et al., "Climate change 2021: The physical science basis," *Contribution Working Group I. 6th Assessment Rep. Intergovernmental Panel Climate Change*, vol. 2, pp. 147–286, 2021.

[2] F. Blaabjerg, Y. Yang, K. A. Kim, and J. Rodriguez, "Power electronics technology for large-scale renewable energy generation," *Proc. IEEE Inst. Electr. Electron. Eng.*, vol. 111, no. 4, pp. 335–355, Apr. 2023.

[3] L. Meegahapola, A. Sguarezi, J. S. Bryant, M. Gu, E. R. C. D., and R. B. A. Cunha, "Power system stability with power-electronic converter interfaced renewable power generation: Present issues and future trends," *Energies*, vol. 13, 2020, Art. no. 3441.

[4] T. Dragicevic, S. Vazquez, and P. Wheeler, "Advanced control methods for power converters in DG systems and microgrids," *IEEE Trans. Ind. Electron.*, vol. 68, no. 7, pp. 5847–5862, Jul. 2021.

[5] J. S. Costa, A. Lunardi, and A. J. S. Filho, "MPC design control modulation using performance map applied to VCS-grid converter with l filter," *Eletrônica de Potência*, vol. 27, 2022.

[6] A. Lunardi, E. Conde, J. Assis, L. Meegahapola, D. A. Fernandes, and A. J. S. Filho, "Repetitive predictive control for current control of grid-connected inverter under distorted voltage conditions," *IEEE Access*, vol. 10, pp. 16931–16941, 2022.

[7] P. Costa, M. Castro, I. Machado, and E. Sa, "Experimental evaluation of a multifunctional system single-stage pv-shunt active filter under partial shading conditions," *Braz. J. Power Electron. (SOBRAEP)*, vol. 25, no. 2, pp. 198–208, 2020.

[8] C. F. Garcia, C. A. Silva, J. R. Rodriguez, P. Zanchetta, and S. A. Odhano, "Modulated model-predictive control with optimized overmodulation," *IEEE Trans. Emerg. Sel. Topics Power Electron.*, vol. 7, no. 1, pp. 404–413, Mar. 2019.

[9] C. Xie, K. Li, J. Zou, D. Liu, and J. M. Guerrero, "Passivity-based design of grid-side current-controlled LCL-type grid-connected inverters," *IEEE Trans. Power Electron.*, vol. 35, no. 9, pp. 9813–9823, Sep. 2020.

[10] R. N. Beres, X. Wang, M. Liserre, F. Blaabjerg, and C. L. Bak, "A review of passive power filters for three-phase grid-connected voltage-source converters," *IEEE Trans. Emerg. Sel. Topics Power Electron.*, vol. 4, no. 1, pp. 54–69, Mar. 2016.

[11] M. Morey, N. Gupta, M. M. Garg, and A. Kumar, "A comprehensive review of grid-connected solar photovoltaic system: Architecture, control, and ancillary services," *Renewable Energy Focus*, vol. 45, pp. 307–330, 2023. [Online]. Available: https://www.sciencedirect.com/science/article/pii/S1755008423000376

[12] J. Hu, Y. Shan, J. M. Guerrero, A. Ioinovici, K. W. Chan, and J. Rodriguez, "Model predictive control of microgrids–An overview," *Renewable Sustain. Energy Rev.*, vol. 136, 2021, Art. no. 110422.

[13] Y. Gui, X. Wang, F. Blaabjerg, and D. Pan, "Control of grid-connected voltage-source converters: The relationship between direct-power control and vector-current control," *IEEE Ind. Electron. Mag.*, vol. 13, no. 2, pp. 31–40, Jun. 2019.

[14] W. Taha, A. R. Beig, and I. Boiko, "Quasi optimum pi controller tuning rules for a grid-connected three phase ac to DC PWM rectifier," *Int. J. Elect. Power Energy Syst.*, vol. 96, pp. 74–85, 2018.

[15] Y. Wu, X. Zhao, K. Li, M. Zheng, and S. Li, "Energy saving–another perspective for parameter optimization of P and PI controllers," *Neurocomputing*, vol. 174, pp. 500–513, 2016.

[16] D. Perez-Estevez, J. Doval-Gandoy, A. G. Yepes, O. Lopez, and F. Baneira, "Generalized multifrequency current controller for grid-connected converters with LCL filter," *IEEE Trans. Ind. Appl.*, vol. 54, no. 5, pp. 4537–4553, Sep./Oct. 2018.

[17] J. Rodriguez and P. Cortes, *Predictive Control of Power Converters and Electrical Drives*. Hoboken, NJ, USA: Wiley2012.

[18] A. J. S. Filho, *Model Predictive Control for Doubly-Fed Induction Generators and Three-Phase Power Converters*. Amsterdam, Netherlands: Elsevier, 2022.

[19] C. Bordons, F. Garcia-Torres, and M. A. Ridao, *Model Predictive Control of Microgrids*. Berlin, Germany: Springer, 2020.

[20] J. A. Rossiter, *Model-Based Predictive Control: A. Practical Approach, Ser. Control Series*. Boca Raton, FL, USA: CRC Press, 2003.

[21] M. Yazdanian and A. Mehrizi-Sani, "Internal model-based current control of the RL filter-based voltage-sourced converter," *IEEE Trans. Energy Convers.*, vol. 29, no. 4, pp. 873–881, Dec. 2014.

[22] N. Narasimhulu, M. Awasthy, R. P. d. Prado, P. B. Divakarachari, and N. Himabindu, "Analysis and impacts of grid integrated photo-voltaic and electric vehicle on power quality issues," *Energies*, vol. 16, no. 2, Jan. 2023, Art. no. 714.

[23] J. Liu, Y. Miura, and T. Ise, "Cost-function-based microgrid decentralized control of unbalance and harmonics for simultaneous bus voltage compensation and current sharing," *IEEE Trans. Power Electron.*, vol. 34, pp. 7397–7410, Aug. 2019.

[24] H. T. Nguyen, J. Kim, and J.-W. Jung, "Improved model predictive control by robust prediction and stability-constrained finite states for three-phase inverters with an output *LC* filter," *IEEE Access*, vol. 7, pp. 12673–12685, 2019.

[25] A. Sufyan et al., "A robust nonlinear sliding mode controller for a three-phase grid-connected inverter with an LCL filter," *Energies*, vol. 15, no. 24, 2022, Art. no. 9428.

[26] B. Sari, M. F. Benkhoris, J. C. L. Claire, and B. Rabhi, "Robust h∞ output feedback control design applied to uninterruptible power supplies," in *Proc. IEEE Int. Symp. Ind. Electron.*, 2012, pp. 490–495.

[27] L. Maccari et al., "Robust h∞ control for grid connected PWM inverters with LCL filters," in *Proc. 10th IEEE/IAS Int. Conf. Ind. Appl.*, 2012, pp. 1–6.

[28] S. P. Ribas, L. A. Maccari Jr., H. Pinheiro, R. C. d. L. F. d. Oliveira, and V. F. Montagner, "Design and implementation of a discrete-time h-infinity controller for uninterruptible power supply systems," *IET Power Electron.*, vol. 7, no. 9, pp. 2233–2241, 2014.

[29] D. A. C. d. Araujo, J. A. M. Neto, T. A. d. Brasil, J. A. Gouvea, and A. R. L. Zachi, "Robust current control of three-phase grid-connected converters by using the ADRC method," in *Proc. Braz. Power Electron. Conf.*, 2021, pp. 1–8.

[30] M. Safonov, "Stability margins of diagonally perturbed multivariable feedback systems," *IEE Proc. D. Control Theory Appl.*, vol. 129, pp. 251–256, 1982.

[31] S. Skogestad and I. Postlethwaite, *Multivariable Feedback Control: Analysis and Design*. Hoboken, NJ, USA: Wiley, 2005.

[32] D.-W. Gu, P. H. Petkov, and M. M. Konstantinov, *Robust Control Design With MATLAB*. Berlin, Germany: Springer2013.

[33] E. R. C. Duque, A. Lunardi, J. S. Solís-Chaves, T. d. S. Paiva, D. A. Fernandes, and A. J. S. Filho, "Improvement of robustness of MPC adding repetitive behavior for the DFIG current control," *Energies*, vol. 15, 2022, Art. no. 4114.

[34] J. S. Costa, A. Lunardi, L. F. N. Lourenço, and A. J. S. Filho, "Robust predictive repetitive current control for a grid-connected inverter under parametric uncertainty," *IEEE Trans. Emerg. Sel. Topics Power Electron.*, vol. 11, no. 5, pp. 4693–4703, Oct. 2023.

[35] J. S. Costa, A. Lunardi, P. C. Ribeiro, I. B. D. Silva, D. A. Fernandes, and A. J. S. Filho, "Performance-based tuning for a model predictive direct power control in a grid-tied converter with l-filter," *IEEE Access*, vol. 11, pp. 8017–8028, 2023.

[36] L. Chen, H. Nian, and Y. Xu, "Improved model predictive direct power control of grid side converter in weak grid using Kalman filter and DSOGI," *Chin. J. Elect. Eng.*, vol. 5, pp. 22–32, 2019.

[37] N. Vázquez and J. V. López, "Inverters," in *Power Electronics Handbook*. Amsterdam, Netherlands: Elsevier, 2018, pp. 289–338.

[38] A. J. S. Filho, M. E. d. O. Filho, and E. R. Filho, "A predictive power control for wind energy," *IEEE Trans. Sustain. Energy*, vol. 2, no. 1, pp. 97–105, Jan. 2011.

[39] R. Panigrahi, S. K. Mishra, S. C. Srivastava, A. K. Srivastava, and N. N. Schulz, "Grid integration of small-scale photovoltaic systems in secondary distribution network—A review," *IEEE Trans. Ind. Appl.*, vol. 56, no. 3, pp. 3178–3195, May-Jun. 2020.

[40] G. Abad, J. Lopez, M. Rodriguez, L. Marroyo, and G. Iwanski, *Doubly Fed Induction Machine: Modeling and Control for Wind Energy Generation*, M. E. El-Hawary, ed. Hoboken, NJ, USA: Wiley, 2011.

[41] A. Lunardi, E. R. C. D, J. d. Assis, D. A. Fernandes, and A. J. S. Filho, "Model predictive control with modulator applied to grid inverter under voltage distorted," *Energies*, vol. 14, 2021, Art. no. 4953.

[42] A. J. S. Filho and E. R. Filho, "Model-based predictive control applied to the doubly-fed induction generator direct power control," *IEEE Trans. Sustain. Energy*, vol. 3, no. 3, pp. 398–406, Jul. 2012.

[43] A. Lunardi, A. S. Filho, C. Capovilla, I. Casella, and A. d. Medeiros, "A wireless coded predictive direct power control for renewable energy sources in smart grid environment," *Int. J. Elect. Power Energy Syst.*, vol. 112, pp. 319–325, 2019.

[44] J. A. Rossiter, *Model-Based Predictive Control*. Boca Raton, FL, USA: CRC Press, 2017.

[45] M. G. Judewicz, S. A. Gonzalez, J. R. Fischer, J. F. Martinez, and D. O. Carrica, "Inverter-side current control of grid-connected voltage source inverters with LCL filter based on generalized predictive control," *IEEE Trans. Emerg. Sel. Topics Power Electron.*, vol. 6, no. 4, pp. 1732–1743, Dec. 2018.

[46] R. Guzman, L. G. d. Vicuna, A. Camacho, J. Miret, and J. M. Rey, "Receding-horizon model-predictive control for a three-phase VSI with an LCL filter," *IEEE Trans. Ind. Electron.*, vol. 66, no. 9, pp. 6671–6680, Sep. 2019.
[47] B. E. Sedhom, M. M. El-Saadawi, A. Y. Hatata, and A. S. Alsayyari, "Hierarchical control technique-based harmony search optimization algorithm versus model predictive control for autonomous smart microgrids," *Int. J. Elect. Power Energy Syst.*, vol. 115, 2020, Art. no. 105511.
[48] H. Das, M. Rahman, S. Li, and C. Tan, "Electric vehicles standards, charging infrastructure, and impact on grid integration: A technological review," *Renewable Sustain. Energy Rev.*, vol. 120, 2020, Art. no. 109618.

JEFFERSON S. COSTA received the B.S. and M.S. degrees in electrical engineering from the Federal University of Pará (UFPA), Tucuruí, Pará, Brazil, in 2013 and 2016, respectively. Since 2021, he has been working toward the Ph.D. degree in energy with the Federal University of ABC (UFABC), Santo André, Brazil. He is currently a Professor with UFPA, Tucuruí, Pará, teaching calculus, electromagnetism, and electrical materials. His research interests include control applied to machine drives, power converters, electric vehicles, and photovoltaic and wind energy.

ANGELO LUNARDI received the degree in electronic engineering from the Instituto Mauá Tecnologia, São Paulo, Brazil, in 2015, the master's degree in electrical engineering from the Universidade Federal do ABC (UFABC), Santo Andé, Brazil, with a focus on control research applied to wind power generation, in 2017, and the Ph.D. degree in electrical engineering from the University of São Paulo, Sã o Paulo, with a thesis titled robust predictive control applied to the converter connected to the grid, in 2022. He is currently a Researcher with the UFABC and works with control systems for renewable energy.

DARLAN ALEXANDRIA FERNANDES (Member, IEEE) received the B.S. degree in electrical engineering from the Federal University of Paraiba, João Pessoa, Brazil, in 2002, and the M.S. and Ph.D. degrees in electrical engineering from the Federal University of Campina Grande, Campina Grande, Brazil, in 2004 and 2008, respectively. He was a Visiting Scholar with the Center for Power Electronics Systems (CPES), Virginia Polytechnic Institute and State University (Virginia Tech), Blacksburg, VA, USA, from 2018 to 2019. From 2007 to 2011, he was a Professor with the Industry Department, Federal Center of Technological Education of Rio Grande do Norte. He is currently an Assistant Professor with the Department of Electrical Engineering, Federal University of Paraiba. His research interests include applications of power electronics in distribution systems, power quality, photovoltaic systems, and Impedance-based control design techniques for static converters.

ALFEU J. SGUAREZI FILHO (Senior Member, IEEE) received the master's and Doctor degrees in electrical engineering from the Faculty of Electrical and Computer Engineering, University of Campinas (Unicamp), Campinas, Brazil, in 2007 and 2010, respectively. He is currently an Associate Professor with the Federal University of ABC, Santo Andre, Brazil. He is the author of several articles in national and international scientific journals and book chapters in the areas of electrical machines, machine drives, electric vehicles, power electronics, wind and photovoltaic energies.